

Absence of heat flow in $\nu = 0$ quantum Hall ferromagnet in bilayer graphene

Received: 27 December 2023

Accepted: 19 September 2024

Published online: 29 October 2024

 Check for updates

Ravi Kumar^{1,4}, Saurabh Kumar Srivastav^{1,4}, Ujjal Roy^{1,4}, Ujjawal Singhal¹, K. Watanabe², T. Taniguchi², Vibhor Singh¹, P. Roulleau³ & Anindya Das¹✉

The charge neutrality point of bilayer graphene, denoted as the $\nu = 0$ state, manifests competing phases marked by spontaneous ordering of the spin, valley and layer degrees of freedom under external magnetic and electric fields. However, due to their electrically insulating nature, identifying these phases through electrical conductance measurements is a challenge. A recent theoretical proposal suggests that thermal transport measurements can detect these competing phases. Here we experimentally show that the bulk thermal transport of the $\nu = 0$ state in bilayer graphene vanishes. This is in contrast to the theory, which predicts a finite thermal conductance in the $\nu = 0$ state. By varying the external electric field and conducting temperature-dependent measurements, our results suggest that there are gapped collective excitations in the $\nu = 0$ state. Our findings underscore the necessity for further investigations into the nature of the $\nu = 0$ state.

The $\nu = 0$ state of the quantum Hall (QH) regime in bilayer graphene (BLG) offers a fertile playground for realizing symmetry-broken many-body ground states that arise from the interplay between the isospin anisotropy of electron–electron and electron–phonon interactions, Zeeman energy and electric field across the layers^{1–13}. The electric field tunability of the isospin ‘layer’ degree of freedom offers an extra knob for exploring the rich phase diagram of the $\nu = 0$ state in BLG^{14–20}. Theoretically, the $\nu = 0$ state is believed to harbour four different ground states¹ with different spin and valley (equivalent to layer or sublattice) degrees of freedom: ferromagnetic (F), canted antiferromagnetic (CAF), partially layer polarized (PLP) and fully layer polarized (FLP). In the F and CAF phases, each electron in a unit cell occupies a different sublattice with the same and canted spin polarization, respectively¹. In the PLP case, both electrons of the unit cell are shared with both the sublattices with opposite spin, and in the FLP state, both electrons occupy the same sublattice (equivalently same layer) with opposite spin polarization. The spin polarization of these phases on different sublattices is schematically shown in Fig. 1a. Although all four phases are electrically insulating in bulk, the ferromagnetic phase is expected to harbour the conducting helical edge modes at the physical boundary of the sample²¹. Similar competing phases are also

expected for the $\nu = 0$ state of monolayer graphene (MLG)². Although several experimental observations based on charge transport measurements support some of the proposed insulating phases in both MLG^{21–29} and BLG^{14–20}, these measurements do not directly capture the spontaneous symmetry breaking of the spin or isospin degrees of freedom.

In contrast to charge transport measurements, thermal transport experiments are believed to be more sensitive in identifying the spontaneous symmetry breaking of spin or isospin degrees of freedom of BLG. For example, heat flows through gapless collective excitations (spin or isospin), like Goldstone modes, of the spontaneously, continuous, symmetry-breaking phases, whereas heat flow is blocked by a gapped spectrum of collective excitations. Indeed, this was proposed by Falko Pientka et al.³⁰, who claimed that at low temperatures, heat can flow through gapless collective modes of the CAF and PLP states but should vanish for the FLP and F phases, where the excitation spectrum is gapped. A similar proposal was also made for MLG^{7,31}. Despite these theoretical predictions, a study of the thermal conductance of the $\nu = 0$ state was lacking due to the technical challenges involved in making thermal transport measurements at low temperatures. We overcame these challenges by successfully developing a thermal conductance measurement technique in the QH regime^{32–34} that employs

¹Department of Physics, Indian Institute of Science, Bangalore, India. ²National Institute of Material Science, Tsukuba, Japan. ³SPEC, CEA, CNRS, Université Paris-Saclay, CEA Saclay, Gif sur Yvette, France. ⁴These authors contributed equally: Ravi Kumar, Saurabh Kumar Srivastav, Ujjal Roy.

✉e-mail: anindya@iisc.ac.in

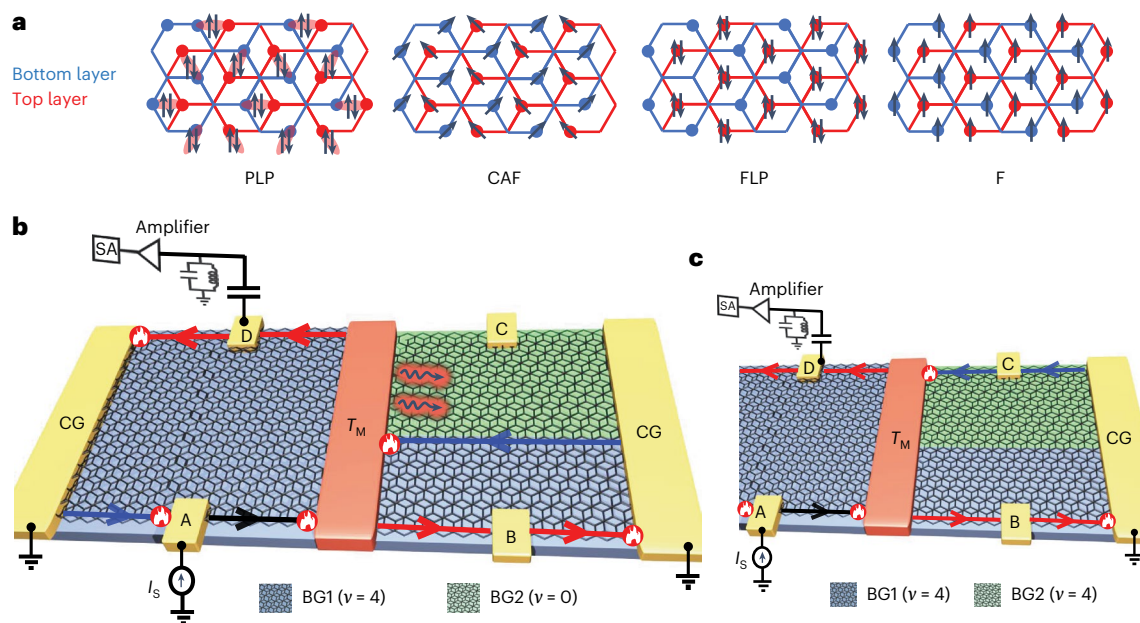


Fig. 1 | $\nu = 0$ ground states of BLG, device schematic and measurement set-up. **a**, $\nu = 0$ QH phase of BLG with the four predicted ground states. **b**, The device and measurement set-up. The device was placed into the integer QH regime. The global BLG part (shown in blue and controlled by a graphite back gate, BG1) was placed into the $\nu = 4$ state. The local BLG part (shown in green and controlled by a local graphite back gate BG2) was placed in the $\nu = 0$ state. For simplicity, four edge channels are shown by a single line with an arrow. A d.c. current I_s was injected from contact A. This current moves in the anticlockwise direction set by the magnetic field. Chiral edge channels (red) at potential $V_M = \frac{I_s}{2} \times \frac{h}{ve^2}$ and temperature T_M leave the floating contact and terminate in two

cold ground contacts (CG), where h and e are Planck constant and charge of an electron, respectively. The electron temperature T_M of the floating contact was determined by measuring the excess thermal noise at contact D at a frequency ≈ 725 kHz using an LCR-resonant circuit, which was followed by a cascade of amplifiers, and it was finally measured by a spectrum analyser (SA). The wiggly line emanating from the floating contact represents heat transport through Goldstone modes of the $\nu = 0$ state. **c**, Same as **b**, but here both the global and local BLG parts are set to $\nu = 4$. The hot spots in **b** and **c** at different corners are shown as red circles filled with a white flame.

Johnson–Nyquist noise to determine the temperature of the heat reservoirs at low temperatures. This technique was used to measure the electronic contribution of heat flow due to chiral edge channels in integer and fractional QH phases in graphene and BLG^{35–39}.

In the spirit of the theoretical proposal of Falko Pientka et al.³⁰, here we report on heat flow in the $\nu = 0$ state in dual-gated BLG devices encapsulated in hexagonal boron nitride (hBN). To measure the thermal conductance, we used a device geometry in which a metallic floating contact reservoir was connected to two independent QH regions, whose filling was controlled by a global graphite back gate^{35–37}. To create a $\nu = 0$ region in this device structure, we employed another local gate such that we could tune our device with and without the $\nu = 0$ state. Further, in the $\nu = 0$ state, the displacement field (D) was varied from $D = 0$ to $D \approx 0.1$ V nm⁻¹ for the expected ground states of CAF and FLP, respectively³⁰. The thermal conductance was measured from very low temperatures, 20 mK to 1 K. At low temperature, in the absence of the $\nu = 0$ state, the measured thermal conductance matched the expected electronic contribution. Next, the device was placed in the $\nu = 0$ state using the local gate, and surprisingly, no further detectable contribution to the thermal conductance was measured, so that the results remained the same irrespective of the external electric field (D) or temperature. This confirms the absence of heat flow in the $\nu = 0$ state from the anticipated collective excitations of isospin.

Device and experimental principle

The device schematic and measurement set-up are shown in Fig. 1b,c. The device consists of hBN-encapsulated BLG placed on two independent graphite back gates. The global graphite back gate BG1 and the local graphite back gate BG2 control the charge carrier density or the filling factors of the blue and green parts in Fig. 1b,c, respectively. Details of

the device structure are given in Supplementary Information Section 1, and there are optical images in Supplementary Fig. 1. Note that we have chosen two graphite back gates so that the $\nu = 0$ state has a zero displacement field (details in Supplementary Information Section 3), which allows it to host the CAF ground state as theoretically suggested³⁰ for a moderate perpendicular magnetic field ($B < 10$ T). The local graphite back gate BG2 was separated from the global graphite back gate BG1 by a thin hBN flake with a thickness of around 10 nm. The contacts on the BLG were patterned into a Hall bar geometry. There was a metallic floating contact in the middle, which was connected to the BLG with one-dimensional edge contacts (see Supplementary Information Section 1 for details). We fabricated two graphite back-gated devices, devices 1 and 2. Device 1 was cooled down to 20 mK in a dilution refrigerator, and a perpendicular field of 4 T was applied. The QH response with robust plateaux at different filling factors can be seen in Supplementary Fig. 2. The electrical conductance was measured with standard lock-in techniques, whereas the thermal conductance was measured with noise thermometry^{35–38} based on an LC-resonant circuit, amplifiers and a spectrum analyser (details in Supplementary Information Section 4). To determine the thermal conductance of the $\nu = 0$ state, we performed measurements for two different cases: (1) when both the global and the local BLG parts had the same filling factor $\nu = 4$ (Fig. 1c) and (2) when the global BLG part had $\nu = 4$ whereas the local BLG part was in the $\nu = 0$ QH state (Fig. 1b). The difference in the thermal conductance values of these two cases provides the thermal conductance of the $\nu = 0$ state. If the gapless collective excitations, like Goldstone modes, exist for the $\nu = 0$ state (Fig. 1b), extra heat current should flow from the hot floating contact to the cold ground in addition to the electronic heat flow through chiral edge channels, as shown schematically in Fig. 1b.

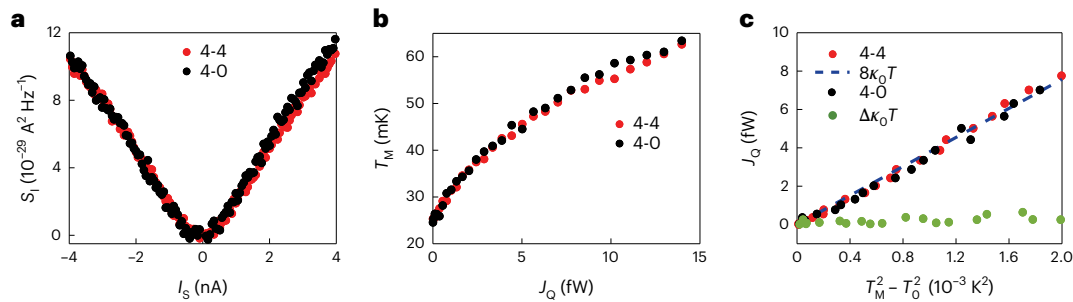


Fig. 2 | Thermal conductance data at the base temperature 20 mK. a, Excess thermal noise S_1 measured as a function of the source current for device 1 for two cases: (1) $v_{\text{BG1}} = 4$ and $v_{\text{BG2}} = 4$ (4-4, red filled circles) and (2) $v_{\text{BG1}} = 4$ and $v_{\text{BG2}} = 0$ (4-0, black filled circles). **b**, Temperature T_M of the floating contact plotted as a

function of the dissipated power J_Q . **c**, J_Q (solid circles) plotted as a function of $T_M^2 - T_0^2$, showing excellent agreement with $G_Q = 8\kappa_0 T$ (dashed blue line). Green solid circles represent the difference in thermal conductance of the two cases (4-4 and 4-0) in units of $\kappa_0 T$ and show no detectable difference.

Heat flow measurement

We first describe the results for case 1 without the $\nu = 0$ state. The whole BLG was set to $\nu = 4$ (Fig. 1c). A d.c. current I_S was injected at contact A, which flowed towards the floating reservoir. The outgoing current from the floating reservoir split into two equal parts (see Supplementary Fig. 2 for details) and flowed towards the cold ground contacts. The power dissipation at the floating reservoir due to hot spots (Joule heating) was $J_Q = \frac{I_S^2}{4\nu G_0}$ (refs. 35–37,39), where G_0 is the quanta of electrical conductance. Thus, the electrons in the floating reservoir reached a new steady-state temperature (T_M) with the following heat balance relation: $J_Q = J_Q^e(T_M, T_0) = 0.5N\kappa_0(T_M^2 - T_0^2)$ (refs. 35–37,39), where $J_Q^e(T_M, T_0)$ is the electronic contribution of the heat current through N chiral edge modes (here, $N = 8$ as four QH edge channels leave the floating reservoir towards the left and four leave towards the right in Fig. 1c), and $\kappa_0 = \pi^2 k_B^2 / 3h$ (refs. 35–37,39) with k_B the Boltzmann constant, h the Planck constant and T_0 the temperature of the cold ground. The T_M of the floating reservoir was obtained by measuring the excess thermal noise at contact D, as given by $S_1 = \nu k_B(T_M - T_0)G_0$ (refs. 35–37,39), along the outgoing edge channels, as shown in Fig. 1. Figure 2a shows the measured excess thermal noise S_1 (red circles) as a function of current I_S for case 1 without the $\nu = 0$ state (at bath temperature $T_{\text{bath}} \approx 20$ mK). The current and the noise axes of Fig. 2a were converted to J_Q and T_M and plotted in Fig. 2b (red circles). To extract the thermal conductance G_Q , we have plotted J_Q as a function of $T_M^2 - T_0^2$ in Fig. 2c. The solid red circles represent the experimental data, and the blue dashed line represents the theoretical contribution of the electronic heat flow for $G_Q = 8\kappa_0 T$, where $T = (T_M + T_0)/2$. The excellent match between the experimentally measured data and theory in Fig. 2c unambiguously proves the accuracy of our measurement set-up.

Now, we will discuss the results obtained for case 2 with the $\nu = 0$ state, where the local BLG part (BG2) was set at $\nu = 0$ while the global BLG part was kept at $\nu = 4$ (Fig. 1b). It could be expected that the electronic contribution to the thermal conductance would remain the same, as the number of electronic channels leaving the floating reservoir has not changed. However, if the gapless collective excitations, like Goldstone modes, existed in the $\nu = 0$ part, then the thermal conductance would be expected to be higher than in case 1 as $J_Q = 0.5N\kappa_0(T_M^2 - T_0^2) + J_Q^{\text{CAF}}(T_M, T_0)$, where $J_Q^{\text{CAF}}(T_M, T_0)$ is the extra heat current carried by the gapless collective excitations (as expected for the CAF phase). The wiggly lines in Fig. 1b represent the extra heat flow through gapless Goldstone modes in the electrically insulating bulk of the $\nu = 0$ state in the local BLG part. The results obtained for case 2 with the $\nu = 0$ state are shown by the solid black circles in Fig. 2a–c. Surprisingly, the results for case 2 with the $\nu = 0$ state are identical to those for case 1 without the $\nu = 0$ state. Moreover, the measured thermal conductance matched extremely well with $8\kappa_0 T$ without any other contribution (Fig. 2c). The measurement was repeated for device 2,

which allowed us to measure another configuration: (1) when both the global and local BLG parts have the same filling factor $\nu = 1$ and (2) when the global BLG part has $\nu = 1$, whereas the local BLG part was in the $\nu = 0$ state. The details are shown in Supplementary Figs. 4 and 5. No other heat flow contribution was observed through the $\nu = 0$ state.

With the two graphite back gates (global and local) in the above device geometry, we could not vary D to access the other phases of the $\nu = 0$ QH state of the local BLG part. To achieve this, we used another type of device structure, device 3, which has a metallic local top gate over the hBN-encapsulated BLG. This structure was isolated from metallic ohmic contacts by a few-nanometre-thick insulating layer of Al_2O_3 , as shown schematically in Fig. 3a. Details can be found in Supplementary Fig. 6. The displacement field (D) was varied for the local BLG part. The effect of D on the $\nu = 0$ state is illustrated in Supplementary Fig. 7g, which shows the closing of the insulating gap of the $\nu = 0$ state around $D^* \approx \pm 0.07$ V nm $^{-1}$. This indicates the transition from one phase of the $\nu = 0$ state to another, as reported in the literature^{14,19,40,41}. Figure 3b,c summarizes the thermal conductance results for device 3 in two scenarios: (1) when both the global and local BLG parts had the same filling factor $\nu = 4$ and (2) when the global BLG part had $\nu = 4$ whereas the local BLG part was tuned to the $\nu = 0$ state with $D \approx -0.08$ V nm $^{-1}$ ($>D^*$). In the latter scenario, no other contribution to the heat flow was observed for the $\nu = 0$ state.

The absence of thermal conductance at a finite $D \approx -0.08$ V nm $^{-1}$ in Fig. 3 for device 3 was expected, as the ground state of the $\nu = 0$ state was FLP with gapped excitations^{1,28,30,40}. However, the absence of heat flow in the $\nu = 0$ state at $D \approx 0$ for devices 1 and 2 (Fig. 2 and Supplementary Fig. 5) was surprising, as the $\nu = 0$ state was expected to be in the CAF phase with gapless excitations³⁰. These results may suggest the following possible scenarios: (1) The ground states of the $\nu = 0$ state did not support the gapless collective excitations or (2) at the lower bath temperature (~ 20 mK), the thermal conductance contribution of the collective excitations was negligible. Next, we discuss the possible ground states of the $\nu = 0$ state and their excitation spectra. Here we focus on the second scenario. This scenario has merit, as the contribution from collective excitations in two dimensions was expected to decrease quadratically with temperature³⁰. To capture a notable contribution from the collective excitations, we conducted measurements at elevated temperatures up to 1 K for both scenarios for device 1: (1) without the $\nu = 0$ state and (2) with the $\nu = 0$ state. However, these higher temperature measurements were challenging due to the potential heat loss through electron–phonon coupling from the hot metallic floating contact to the substrate as well as due to heat loss to phonons in the BLG from the hot metallic floating contact to the cold ground.

To simplify the analysis, we restricted our measurements to the linear regime at elevated temperatures, while ensuring that $\Delta T < T_0$, where $\Delta T = (T_M - T_0)$ and T_0 is the temperature of the cold ground. In this regime, the heat balance equation can be simplified as follows: $J_Q = 0.5N\kappa_0(T_M^2 - T_0^2) + G_Q^{\text{CAF}}\Delta T + G_Q^{\text{ph}}\Delta T + C_Q^{\text{e-ph}}\Delta T$. This can

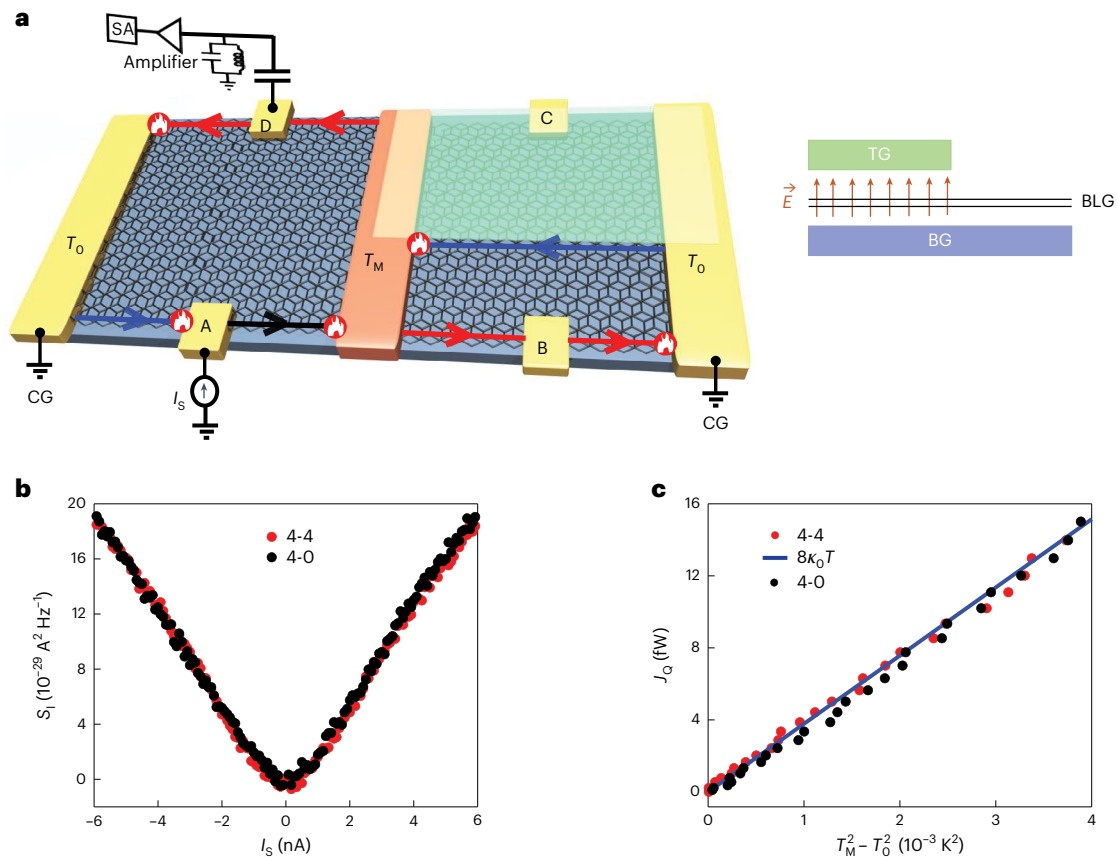


Fig. 3 | Thermal transport at finite D . **a**, Device schematic. The device is the same as the one in Fig. 1b, except that BG2 has been replaced by a top gate (TG) to apply a transverse displacement field, as shown schematically in the right-hand panel. **b**, Excess thermal noise S_1 measured as a function of the source current for two

cases: (1) $v_{BG} = 4$ and $v_{TG} = 4$ (red) and (2) $v_{BG} = 4$ and $v_{TG} = 0$ (black) at $D \approx -0.08 \text{ V nm}^{-1}$ (see Supplementary Fig. 7 for details). **c**, J_Q (solid circles) as a function of $T_M^2 - T_0^2$. The blue solid line represents the linear fit with $G_Q = 8k_0 T$.

be simplified to $J_Q = Nk_0 T_0 \Delta T + G_Q^{\text{CAF}} \Delta T + G_Q^{\text{ph}} \Delta T + G_Q^{\text{e-ph}} \Delta T$, where the successive terms represent contributions from electronic channels, collective excitations (CAF), phonons and electron–phonon interactions, respectively. Figure 4a–c shows the measured excess thermal noise S_1 as a function of injected current I_s at $T_{\text{bath}} = 80, 300$ and 500 mK for the two scenarios with and without the $\nu = 0$ state. We did not observe any difference between the two cases. In Fig. 4d–f, J_Q versus ΔT is plotted at $T_{\text{bath}} = 80, 300$ and 500 mK for one of the scenarios. Over a small ΔT range ($\Delta T < T_0$), J_Q increased linearly with ΔT . The slope gives the value of the thermal conductance, as indicated by the solid blue lines. The solid black lines show the expected contribution from the electronic edge channels ($Nk_0 T \approx 8k_0 T_0$). Unlike at low temperatures (Fig. 2), at elevated temperatures, the measured thermal conductance was much higher than the electronic part, as expected from the extra contributions. However, the absence of any detectable difference between the two scenarios, with and without the $\nu = 0$ state in Fig. 4a–c, suggests that there was no heat flow due to collective excitations of isospins in the $\nu = 0$ QH ferromagnet of BLG. Note that the cooling of the electron system remained efficient down to our lowest bath temperature. The electron temperature T_0 remained very close to T_{bath} throughout the entire temperature range of our measurements. At the lowest $T_{\text{bath}} \approx 20$ mK, $T_0 \approx 24$ mK. Details are shown in Supplementary Information Section 5 and can be found in our previous work^{35,37,38}.

To clarify our findings at elevated temperatures, as depicted in Fig. 4, we analysed the two-dimensional heat current flowing through collective excitations. At lower temperatures, it is reasonable to assume that heat transport occurred ballistically through collective excitations of isospin or phonons³⁰. For linearly dispersive excitations, the thermal

conductance can be expressed approximately as Wv^2/ν (ref. 30), where W and ν represent the width of the device and the velocity of the excitations, respectively. In Fig. 5, we have plotted the extra contribution to the thermal conductance (extracted from the measured total thermal conductance in Fig. 4, excluding the electronic part) as a function of the bath temperature, using solid circles. The data are fitted well by $2.7 \times 10^{-9} \times T^{2.5}$, as indicated by the solid black line. The power exponent of around 2 implies that the extra contribution to the thermal conductance arose from collective excitations. However, the absence of a discernible difference between scenario 1 without the $\nu = 0$ state and scenario 2 with the $\nu = 0$ state suggests that the primary origin of the extra contribution at the elevated temperature was from phonons (G_Q^{ph}). Note that the thermal conductance from ballistic phonons was expected to exhibit a T^2 dependence. However, the observed power exponent of greater than 2 suggests the influence of electron–phonon coupling ($G_Q^{\text{e-ph}}$), which facilitated heat loss from the hot electrons of the floating metal to the phonons within the metal. The $G_Q^{\text{e-ph}}$ was anticipated to have a higher power exponent (T^α , where $\alpha \approx 4-5$)³⁵. Additionally, the quadratically dispersive flexural modes of graphene can result in different power dependencies. Future studies are necessary to fully understand the power exponent at elevated temperatures.

Discussion

According to ref. 1, the four ground states of the $\nu = 0$ state are CAF, PLP, FLP and F. Among these, the excitations remain gapped for FLP and F, whereas CAF and PLP are expected to support gapless collective excitations, as suggested by ref. 30. Notably, around $T_0 \approx 100$ mK, the thermal conductance from the gapless collective excitations is nearly

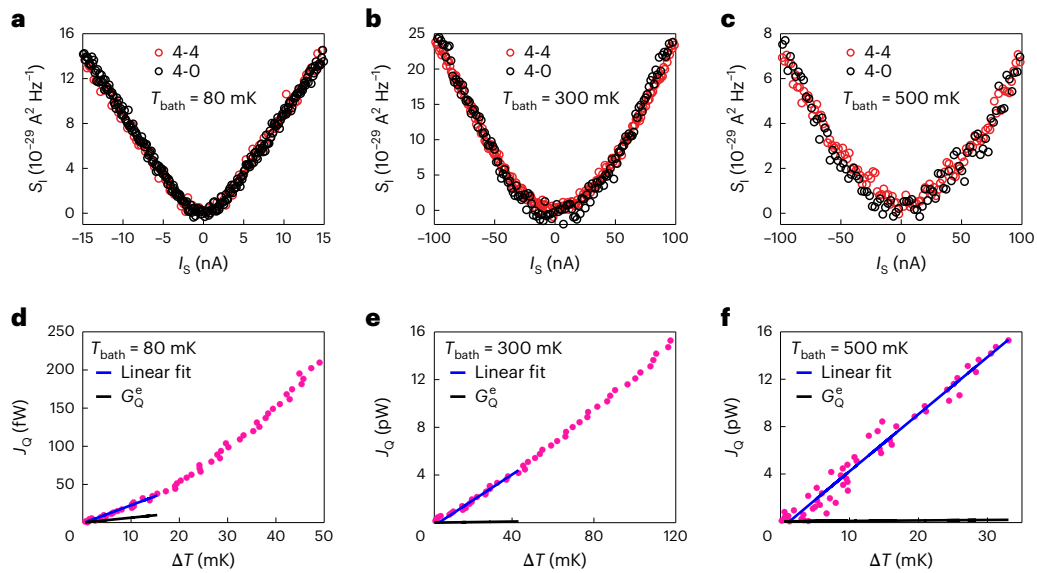


Fig. 4 | Thermal conductance data at higher temperatures. **a–c**, Excess thermal noise S_1 measured as a function of the source current at temperatures 80 mK (**a**), 300 mK (**b**) and 500 mK (**c**) for device 1 for two cases: (1) $\nu_{\text{BG1}} = 4$ and $\nu_{\text{BG2}} = 4$ (red) and (2) $\nu_{\text{BG1}} = 4$ and $\nu_{\text{BG2}} = 0$ (black). **d–f**, For case 2 (4-0), J_Q versus

ΔT plotted for 80 mK (**d**), 300 mK (**e**) and 500 mK (**f**). To calculate the thermal conductance, the data were fitted linearly (solid blue line) in a small ΔT range. The solid black line represents the expected electronic contribution of the thermal conductance.

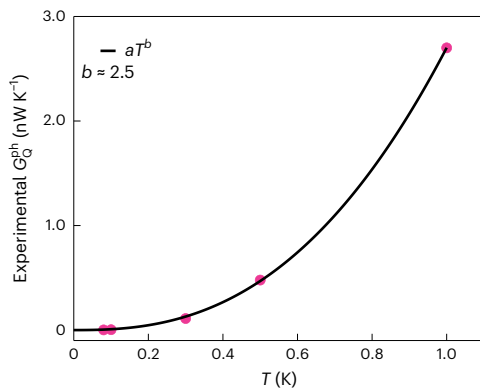


Fig. 5 | Contribution of phonons. Further contribution of thermal conductance as a function of bath temperature, shown in red solid circles. The solid black line is the best fit with $T^{2.5}$.

twice that of an electronic edge channel³⁰ (Supplementary Information Section 8). Therefore, the absence of any thermal conductance in the $\nu = 0$ state in devices 1 and 2 suggests the following scenarios (details in Supplementary Information Sections 6 and 7):

- (1) The ground state could be either FLP or F. However, the electrically insulating nature of the $\nu = 0$ state rules out the F phase. The FLP phase is also unlikely, as the measurements were conducted at zero displacement field, and the BLG was not aligned with the hBN substrate^{1,30}, as indicated by the temperature-dependent resistance data (Supplementary Fig. 3).
- (2) The ground state could be CAF, which was the phase most expected for our devices based on existing transport experiments^{14,28,40} and theories^{1,30}. However, recent scanning tunnelling microscopy experiments^{29,42,43} suggest that the phase could be PLP or even a coexistence of CAF+PLP, as suggested by recent theories⁵. Although ref. 30 indicates that collective excitations for the PLP phase are gapless, higher-order interactions are expected to break the U(1) valley symmetry down to C3, thereby gapping the would-be Goldstone mode^{5,13,44}. For the same reason, a gapped

spectrum was also expected for the coexistence CAF+PLP phase⁵.

- (3) If the ground state is the CAF phase, gapless excitations would be anticipated due to spontaneously broken continuous symmetry. However, the spectrum of CAF may be gapped due to the quantization of collective modes arising from the finite size of the device, an effect observed in BLG devices²⁸. The upper limit of the gap due to this confinement could be as substantial as 350–650 mK for our device dimensions (see Supplementary Information Section 8 for details).
- (4) There might be insufficient coupling between the hot electron bath of the metal and the collective excitations of BLG. However, this is unlikely for our devices, as the metal contacts tend to locally n-dope the BLG flake^{45–47}. Thus, the hot electrons of the reservoir extend into the BLG, potentially enhancing the coupling to collective excitations. For instance, the local n-doping confines the edge channels near the contacts, and the tunnelling of electrons between edge channels with opposite spin can generate and absorb collective excitations. Details can be found in Supplementary Information Section 9.

Therefore, it is most probable that the gap in the excitation spectra of the PLP phase (due to C3 symmetry breaking) or the CAF phase (due to quantization from finite size) inhibited heat transport, resulting in the absence of thermal conductance at lower temperatures. At elevated temperatures, these gaps could be overcome. However, at higher temperatures, phonons become dominant, as illustrated in Fig. 5. At 1 K, the phonon contribution is more than an order of magnitude greater than the expected contribution from the collective excitations of the CAF phase³⁰. A similar experiment conducted with MLG⁴⁸ also found that the bulk heat flow vanished in the $\nu = 0$ state, suggesting an analogy between MLG and BLG. These findings point to potential commonalities in the absence of heat flow in the $\nu = 0$ state in both MLG and BLG, highlighting the need for further theoretical and experimental efforts to fully understand the nature of excitations in the $\nu = 0$ states of MLG and BLG.

Conclusion

In conclusion, our study explored thermal transport measurements of the $\nu = 0$ QH ferromagnet state in BLG by varying the bath temperature

under different displacement fields. The absence of a notable contribution to thermal conductance from the $\nu = 0$ state at zero displacement field suggests the presence of gapped excitations in the device. This work demonstrates the importance of thermal transport measurement for exploring electrically insulating ground states and their collective excitations in bulk phases within the integer and the fractional QH regimes.

Online content

Any methods, additional references, Nature Portfolio reporting summaries, source data, extended data, supplementary information, acknowledgements, peer review information; details of author contributions and competing interests; and statements of data and code availability are available at <https://doi.org/10.1038/s41567-024-02673-z>.

References

- Kharitonov, M. Canted antiferromagnetic phase of the $\nu = 0$ quantum Hall state in bilayer graphene. *Phys. Rev. Lett.* **109**, 046803 (2012).
- Kharitonov, M. Phase diagram for the $\nu = 0$ quantum Hall state in monolayer graphene. *Phys. Rev. B* **85**, 155439 (2012).
- Nomura, K. & MacDonald, A. H. Quantum Hall ferromagnetism in graphene. *Phys. Rev. Lett.* **96**, 256602 (2006).
- Hegde, S. S. & Villadiago, I. S. Theory of competing charge density wave, Kekulé, and antiferromagnetically ordered fractional quantum Hall states in graphene aligned with boron nitride. *Phys. Rev. B* **105**, 195417 (2022).
- Das, A., Kaul, R. K. & Murthy, G. Coexistence of canted antiferromagnetism and bond order in $\nu = 0$ graphene. *Phys. Rev. Lett.* **128**, 106803 (2022).
- Atteia, J. & Goerbig, M. O. $Su(4)$ spin waves in the $\nu = \pm 1$ quantum Hall ferromagnet in graphene. *Phys. Rev. B* **103**, 195413 (2021).
- de Nova, J. & Zapata, I. Symmetry characterization of the collective modes of the phase diagram of the $\nu = 0$ quantum Hall state in graphene: mean-field phase diagram and spontaneously broken symmetries. *Phys. Rev. B* **95**, 165427 (2017).
- Wu, F., Sodemann, I., Araki, Y., MacDonald, A. H. & Jolicœur, T. $So(5)$ symmetry in the quantum Hall effect in graphene. *Phys. Rev. B* **90**, 235432 (2014).
- Goerbig, M. Electronic properties of graphene in a strong magnetic field. *Rev. Mod. Phys.* **83**, 1193 (2011).
- Jung, J. & MacDonald, A. Theory of the magnetic-field-induced insulator in neutral graphene sheets. *Phys. Rev. B* **80**, 235417 (2009).
- Fertig, H. & Brey, L. Luttinger liquid at the edge of undoped graphene in a strong magnetic field. *Phys. Rev. Lett.* **97**, 116805 (2006).
- Alicea, J. & Fisher, M. P. Graphene integer quantum Hall effect in the ferromagnetic and paramagnetic regimes. *Phys. Rev. B* **74**, 075422 (2006).
- Khanna, U. et al. Phase diagram of the $\nu = 2$ quantum Hall state in bilayer graphene. *Phys. Rev. B* **108**, L041107 (2023).
- Maher, P. et al. Evidence for a spin phase transition at charge neutrality in bilayer graphene. *Nat. Phys.* **9**, 154–158 (2013).
- Lee, K. et al. Chemical potential and quantum Hall ferromagnetism in bilayer graphene. *Science* **345**, 58–61 (2014).
- Hunt, B. et al. Direct measurement of discrete valley and orbital quantum numbers in bilayer graphene. *Nat. Commun.* **8**, 948 (2017).
- Velasco Jr, J. et al. Transport spectroscopy of symmetry-broken insulating states in bilayer graphene. *Nat. Nanotechnol.* **7**, 156–160 (2012).
- Martin, J., Feldman, B. E., Weitz, R. T., Allen, M. T. & Yacoby, A. Local compressibility measurements of correlated states in suspended bilayer graphene. *Phys. Rev. Lett.* **105**, 256806 (2010).
- Weitz, R. T., Allen, M. T., Feldman, B. E., Martin, J. & Yacoby, A. Broken-symmetry states in doubly gated suspended bilayer graphene. *Science* **330**, 812–816 (2010).
- Feldman, B. E., Martin, J. & Yacoby, A. Broken-symmetry states and divergent resistance in suspended bilayer graphene. *Nat. Phys.* **5**, 889–893 (2009).
- Young, A. et al. Tunable symmetry breaking and helical edge transport in a graphene quantum spin Hall state. *Nature* **505**, 528–532 (2014).
- Abanin, D. A. et al. Dissipative quantum Hall effect in graphene near the Dirac point. *Phys. Rev. Lett.* **98**, 196806 (2007).
- Checkelsky, J. G., Li, L. & Ong, N. Zero-energy state in graphene in a high magnetic field. *Phys. Rev. Lett.* **100**, 206801 (2008).
- Amet, F., Williams, J., Watanabe, K., Taniguchi, T. & Goldhaber-Gordon, D. Insulating behavior at the neutrality point in single-layer graphene. *Phys. Rev. Lett.* **110**, 216601 (2013).
- Zibrov, A. et al. Even-denominator fractional quantum Hall states at an isospin transition in monolayer graphene. *Nat. Phys.* **14**, 930–935 (2018).
- Stepanov, P. et al. Long-distance spin transport through a graphene quantum Hall antiferromagnet. *Nat. Phys.* **14**, 907–911 (2018).
- Veyrat, L. et al. Helical quantum Hall phase in graphene on $SrTiO_3$. *Science* **367**, 781–786 (2020).
- Fu, H., Huang, K., Watanabe, K., Taniguchi, T. & Zhu, J. Gapless spin wave transport through a quantum canted antiferromagnet. *Phys. Rev. X* **11**, 021012 (2021).
- Coissard, A. et al. Imaging tunable quantum Hall broken-symmetry orders in graphene. *Nature* **605**, 51–56 (2022).
- Pientka, F., Waissman, J., Kim, P. & Halperin, B. I. Thermal transport signatures of broken-symmetry phases in graphene. *Phys. Rev. Lett.* **119**, 027601 (2017).
- Takei, S., Yacoby, A., Halperin, B. I. & Tserkovnyak, Y. Spin superfluidity in the $\nu = 0$ quantum Hall state of graphene. *Phys. Rev. Lett.* **116**, 216801 (2016).
- Jezouin, S. et al. Quantum limit of heat flow across a single electronic channel. *Science* **342**, 601–604 (2013).
- Banerjee, M. et al. Observed quantization of anyonic heat flow. *Nature* **545**, 75 (2017).
- Banerjee, M. et al. Observation of half-integer thermal Hall conductance. *Nature* **559**, 205 (2018).
- Srivastav, S. K. et al. Universal quantized thermal conductance in graphene. *Sci. Adv.* <https://doi.org/10.1126/sciadv.aaw5798> (2019).
- Srivastav, S. K. et al. Vanishing thermal equilibration for hole-conjugate fractional quantum Hall states in graphene. *Phys. Rev. Lett.* **126**, 216803 (2021).
- Srivastav, S. K. et al. Determination of topological edge quantum numbers of fractional quantum Hall phases by thermal conductance measurements. *Nat. Commun.* **13**, 5185 (2022).
- Kumar, R. et al. Observation of ballistic upstream modes at fractional quantum Hall edges of graphene. *Nat. Commun.* **13**, 213 (2022).
- Le Breton, G. et al. Heat equilibration of integer and fractional quantum Hall edge modes in graphene. *Phys. Rev. Lett.* **129**, 116803 (2022).
- Li, J. et al. Metallic phase and temperature dependence of the $\nu = 0$ quantum Hall state in bilayer graphene. *Phys. Rev. Lett.* **122**, 097701 (2019).
- Kuiri, M. & Das, A. Energetics of the complex phase diagram of a tunable bilayer graphene probed by quantum capacitance. *Phys. Rev. B* **99**, 125411 (2019).
- Liu, X. et al. Visualizing broken symmetry and topological defects in a quantum Hall ferromagnet. *Science* **375**, 321–326 (2022).
- Li, S.-Y., Zhang, Y., Yin, L.-J. & He, L. Scanning tunneling microscope study of quantum Hall isospin ferromagnetic states in the zero Landau level in a graphene monolayer. *Phys. Rev. B* **100**, 085437 (2019).

44. Peterson, M. R. & Nayak, C. Effects of Landau level mixing on the fractional quantum Hall effect in monolayer graphene. *Phys. Rev. Lett.* **113**, 086401 (2014).
45. Wei, D. S. et al. Electrical generation and detection of spin waves in a quantum Hall ferromagnet. *Science* **362**, 229–233 (2018).
46. Assouline, A. et al. Excitonic nature of magnons in a quantum Hall ferromagnet. *Nat. Phys.* **17**, 1369–1374 (2021).
47. Kumar, R. et al. Electrical noise spectroscopy of magnons in a quantum Hall ferromagnet. *Nat. Commun.* **15**, 4998 (2024).
48. Delagrangé, R. et al. Vanishing bulk heat flow in the $\nu = 0$ quantum Hall ferromagnet in monolayer graphene. *Nat. Phys.* <https://doi.org/10.1038/s41567-024-02672-0> (2024).
49. Pizzocchero, F. et al. The hot pick-up technique for batch assembly of van der Waals heterostructures. *Nat. Commun.* **7**, 11894 (2016).
50. Wang, L. et al. One-dimensional electrical contact to a two-dimensional material. *Science* **342**, 614–617 (2013).

Publisher's note Springer Nature remains neutral with regard to jurisdictional claims in published maps and institutional affiliations.

Springer Nature or its licensor (e.g. a society or other partner) holds exclusive rights to this article under a publishing agreement with the author(s) or other rightsholder(s); author self-archiving of the accepted manuscript version of this article is solely governed by the terms of such publishing agreement and applicable law.

© The Author(s), under exclusive licence to Springer Nature Limited 2024

Method

Device fabrication and measurement scheme

In our experiment, an encapsulated device (heterostructure of hBN/BLG/hBN/graphite/hBN/graphite) was made using the standard dry-transfer pick-up technique⁴⁹. Fabrication of this heterostructure involved the mechanical exfoliation of hBN and graphite crystals onto an oxidized silicon wafer using the widely used the Scotch tape technique. First, a hBN sample of thickness ~25–35 nm was picked up at 90 °C using a polydimethylsiloxane stamp coated with poly(bisphenol A carbonate) and placed on a glass slide that was attached to the tip of a home-built micromanipulator. This hBN flake was placed on top of the previously exfoliated BLG. The BLG was picked up at 90 °C. The next step involved picking up the bottom hBN layer (~30–50 nm). Following the previous process, this bottom hBN was picked up using the previously picked-up hBN/BLG. Following the previous step, this hBN/BLG/hBN heterostructure was used to pick up the graphite flake (which acted as the local gate in the device). This heterostructure (hBN/BLG/hBN/graphite) was used to pick up another hBN flake, which was followed by picking up another graphite flake (which acted as a global gate). Finally, the heterostructure was dropped onto the top of an oxidized silicon wafer of thickness 285 nm at a temperature of 180 °C. To remove the residues of the poly(bisphenol A carbonate), this final stack was cleaned in chloroform (CHCl₃) overnight followed by cleaning in acetone and isopropyl alcohol. After this, a poly(methyl methacrylate) photoresist was coated onto this heterostructure to define the contact regions in the Hall probe geometry using electron-beam lithography. Apart from the conventional Hall probe geometry, we defined a region of ~5.5 μm² area in the middle of the BLG flake, which acted as a floating metallic reservoir upon edge contact metallization. After the electron-beam lithography, reactive ion etching (mixture of CHF₃ and O₂ gas with flow rates of 40 and 4 sccm, respectively at 25 °C with a radio-frequency power of 60 W) was used to define the edge contact⁵⁰. The etching time was optimized such that the bottom hBN layer did not etch completely to isolate the contacts from graphite flakes, which were used as gates. Finally, Cr/Pd/Au (4/12/70 nm) was thermally deposited in an evaporator chamber under a base pressure of ~1–2 × 10⁻⁷ mbar. After deposition, a lift-off procedure was performed in hot acetone and isopropyl alcohol. This resulted in a Hall bar device with the floating metallic reservoir connected to both sides of the BLG by the edge contacts. The device's schematics and measurement set-up are shown in Fig. 1b. The distance from the floating contact to the ground contacts was ~5 μm (see Supplementary Information Section 1 for optical images).

For the device structure with a metallic top gate, a hBN/BLG/hBN/graphite heterostructure was created. Standard Hall bar geometry with a metallic floating contact in the middle was fabricated. Finally, a 5-nm-thick oxide layer of Al₂O₃ was evaporated onto the device, followed by deposition of aluminium metal, which acted as the local top gate. All measurements were done in a cryo-free dilution refrigerator at a base temperature of ~20 mK. The electrical conductance was measured using the standard lock-in technique, whereas the thermal conductance was measured with noise thermometry based on an LCR-resonant circuit at a resonance frequency of ~725 kHz. The

signal was amplified by a home-made preamplifier at 4 K followed by a room-temperature amplifier, and finally measured by a spectrum analyser. Details of the measurement technique are discussed in the Supplementary Information Sections 4 and 5. The QH responses of the three devices are shown in Supplementary Information Section 2.

Data availability

The data presented in the manuscript are available from the corresponding author upon request.

Acknowledgements

We thank A. Das for useful discussions. A.D. is thankful for financial support from the Indo-French Centre for the Promotion of Advanced Research (Grant No. SP/IFCP-22-0005). A.D. also thanks the Department of Science and Technology and the Science and Engineering Research Board, India, for financial support (SP/SERB-22-0387) and acknowledges the Swarnajayanti Fellowship (DST/SJF/PSA-03/2018-19). A.D. also acknowledges funding through the Intensification of Research in High Priority Areas programme of the Science and Engineering Research Board (Grant No. IPA/2020/000034). K.W. and T.T. acknowledge support from the Elemental Strategy Initiative conducted by the Ministry of Education, Culture, Sports, Science and Technology, Japan, the CREST (Core Research for Evolutional Science and Technology) (JPMJCR15F3), and the Japan Science and Technology Agency.

Author contributions

R.K., S.K.S. and U.R. contributed to device fabrication and data acquisition and analysis. A.D. contributed to conceiving the idea, to designing the experiment and to data interpretation and analysis. K.W. and T.T. synthesized the hBN single crystals. U.S. and V.S. contributed to Al₂O₃ film deposition and discussions. P.R. contributed to the discussions and data interpretation. All authors contributed to writing the manuscript.

Competing interests

The authors declare no competing interests.

Additional information

Supplementary information The online version contains supplementary material available at <https://doi.org/10.1038/s41567-024-02673-z>.

Correspondence and requests for materials should be addressed to Anindya Das.

Peer review information *Nature Physics* thanks Ganpathy Murthy, Haoxin Zhou and the other, anonymous, reviewer(s) for their contribution to the peer review of this work.

Reprints and permissions information is available at www.nature.com/reprints.